SIAM J. SCI. COMPUT.
Vol. 29, No. 6, pp. 2381–2401

ADAPTIVE SEMIDISCRETE CENTRAL-UPWIND SCHEMES FOR NONCONVEX HYPERBOLIC CONSERVATION LAWS*

ALEXANDER KURGANOV†, GUERGANA PETROVA‡, AND BOJAN POPOV‡

Abstract. We discover that the choice of a piecewise polynomial reconstruction is crucial in computing solutions of nonconvex hyperbolic (systems of) conservation laws. Using semidiscrete central-upwind schemes, we illustrate that the obtained numerical approximations may fail to converge to the unique entropy solution or the convergence may be so slow that achieving a proper resolution would require the use of (almost) impractically fine meshes. For example, in the scalar case, all computed solutions seem to converge to solutions that are entropy solutions for some entropy pairs. However, in most applications, one is interested in capturing the unique (Kruzhkov) solution that satisfies the entropy condition for all convex entropies. We present a number of numerical examples that demonstrate the convergence of the solutions, computed with the dissipative second-order minmod reconstruction, to the unique entropy solution. At the same time, more compressive and/or higher-order reconstructions may fail to resolve composite waves, typically present in solutions of nonconvex conservation laws, and thus may fail to recover the Kruzhkov solution. In this paper, we propose a simple and computationally inexpensive adaptive strategy that allows us to simultaneously capture the unique entropy solution and to achieve a high resolution of the computed solution. We use the dissipative minmod reconstruction near the points where convexity changes and utilize a fifth-order weighted essentially nonoscillatory (WENO5) reconstruction in the rest of the computational domain. Our numerical examples (for one- and two-dimensional scalar and systems of conservation laws) demonstrate the robustness, reliability, and nonoscillatory nature of the proposed adaptive method.

Key words. hyperbolic systems of conservation laws, semidiscrete central-upwind schemes, piecewise polynomial reconstructions, nonconvex flux

AMS subject classification. Primary, 65M12; Secondary, 35L65

DOI. 10.1137/040614189

1. Introduction.

We consider initial-value problems (IVPs) for hyperbolic (systems of) conservation laws in one and two space dimensions:

$$\mathbf{u}_t + \nabla_{\mathbf{x}} \cdot \mathbf{f}(\mathbf{u}) = \mathbf{0}, \tag{1.1}$$

$$\mathbf{u}(\mathbf{x}, 0) = \mathbf{u}_0(\mathbf{x}), \tag{1.2}$$

whose entropy solutions may admit composite waves. Such examples are scalar conservation laws with nonconvex fluxes and systems of conservation laws, for which (at least) one of the structure coefficients, defined in (2.7) in section 2, changes sign. Further, we refer to all these cases as *nonconvex* hyperbolic (systems of) conservation laws.

An important example of such a system is the Euler equations of gas dynamics with a nonconvex equation of state (EOS). In general, in this case, anomalous wave structure should be expected near a phase transition, because the wave speed need

*Received by the editors August 30, 2004; accepted for publication (in revised form) February 20, 2007; published electronically October 17, 2007.

http://www.siam.org/journals/sisc/29-6/61418.html

†Mathematics Department, Tulane University, New Orleans, LA 70118 (kurganov@math.tulane.edu). This author's work was supported in part by NSF grants DMS-0310585 and DMS-0610430.

‡Department of Mathematics, Texas A&M University, College Station, TX 77843 (gpetrova@math.tamu.edu, popov@math.tamu.edu). The work of the second author was supported in part by NSF grants DMS-0296020 and DMS-0505501. The work of the third author was supported in part by NSF grant DMS-0510650.

not be monotonic along Hugoniot loci and isentropes, and the usual construction of the wave curves for the Riemann problem must be modified (see [27] and the references therein). Another important example of a nonconvex system of conservation laws is the polymer system used to model polymer flooding processes in enhanced oil recovery (see, e.g., [29]). The solution of the Riemann problem for these two systems is known (see, for example, [2], [23], [24], [27], [36], [38], [39], and [11], [13], respectively). However, designing reliable and robust high-order numerical methods for general initial data remains a challenging problem.

Many classical numerical schemes have been extended to solve nonconvex (systems of) conservation laws. We refer the reader to [1], [4], [5], [6], [10], [31], [37], [40] for several upwind Godunov-type schemes based on both the exact and approximate Riemann problem solvers. A low dissipative front tracking method for the polymer system was proposed in [9]. At the same time, note that the "simplest" extensions of the Roe scheme typically cannot be applied in practice to nonconvex systems of conservation laws. We would also like to point out that many of the aforementioned schemes may require computationally expensive evaluation of integrals or a very careful estimation of the CFL number, since otherwise the computed solution may converge to a weak solution that is not the unique entropy solution (see, for example, [19]).

In this paper, we apply the Godunov-type semidiscrete central-upwind schemes from [15] to numerically solve nonconvex hyperbolic (systems of) conservation laws. These schemes are an attractive alternative to other existing methods because they are simple (no Riemann problem solvers are employed), universal, and efficient, and can be used as a "black-box solver." They consist of three steps: projection (averaging), a piecewise polynomial reconstruction, and evolution of the reconstructed interpolant to the next time level according to the integral form of the conservation law (obtained by integrating (1.1) over the control volume). Assuming the exact averaging and evolution operators are used, the nonoscillatory nature of the computed solution is guaranteed provided the piecewise polynomial reconstruction is nonoscillatory, which is typically achieved with the help of nonlinear limiters. When solving the nonconvex problem (1.1)–(1.2) using the semidiscrete central-upwind schemes from [15], necessary adjustments, related to the estimation of the local speeds of propagation, have to be made. Moreover, it turns out that the choice of reconstruction is crucial for capturing of the unique entropy solution. One may expect that, as in the convex case, the use of more compressive and/or higher-order reconstruction will result in sharper resolution of the computed solution. However, this is not the case here, where sharper reconstructions may lead to the convergence of the computed solutions toward a weak solution, which satisfies the entropy condition for only some, but not all, convex entropies. At the same time, the use of more dissipative reconstructions typically results in computing the unique entropy solution, but with relatively low resolution. For example, the implementation of the dissipative minmod reconstruction (see, e.g., [35], [22], [28], [34]) seems to ensure the convergence toward the unique entropy solution, while more compressible reconstructions based on the generalized minmod [22], [28], [34] or superbee [22], [30], [34] limiters as well as the fifth-order essentially nonoscillatory (WENO5) [3], [12], [26], [32], [33] reconstruction may lead to capturing another weak solution (at least in the case when the mesh is of the reasonably coarse size typically used in practical computations).

In this paper, we introduce a simple scheme adaption strategy for solving nonconvex problems, which utilizes the advantages of both the compressive/high-order and the dissipative reconstructions, namely, computing the entropy solution with high

resolution. This is achieved by the proposed *adaptive semidiscrete central-upwind scheme*. In the new scheme, the choice of reconstruction is based on the so far computed solution and switches adaptively from one type to another at or near the points where the flux convexity changes.

The paper is organized as follows. In section 2, we briefly describe the semidiscrete central-upwind schemes. Several piecewise polynomial reconstructions and their impact on the computed solutions are discussed in section 3. Our scheme adaption strategy is presented in section 4. The numerical examples are shown in section 5, where we test our method on one-dimensional (1-D) and two-dimensional (2-D) nonconvex conservation laws, including scalar equations, the Euler equations of gas dynamics, and the polymer system.

2. Semidiscrete central-upwind schemes—an overview. In this section, we briefly describe the semidiscrete central-upwind schemes proposed in [15]. Here we emphasize the details needed for their implementation for nonconvex conservation laws.

For simplicity, we will focus on the 1-D case, where we consider a uniform spatial grid $x_\alpha = \alpha\Delta x$, and assume that the computed cell averages of the solution at some time level t,

$$\bar{\mathbf{u}}_j(t) \approx \frac{1}{\Delta x}\int_{x_{j-\frac{1}{2}}}^{x_{j+\frac{1}{2}}} \mathbf{u}(x,t)\,dx,$$

are already available. Using these values, we reconstruct a (nonoscillatory) piecewise polynomial interpolant (from now on, we will omit the time-dependence of all computed and reconstructed quantities), $\sum_j \mathbf{p}_j(x)\chi_j(x)$, where χ_j is the characteristic function of $[x_{j-\frac{1}{2}}, x_{j+\frac{1}{2}}]$ and $\mathbf{p}_j(x)$ are the corresponding polynomial pieces. For example, conservative linear pieces have the following form:

$$\mathbf{p}_j(x) = \bar{\mathbf{u}}_j + \mathbf{s}_j(x - x_j). \tag{2.1}$$

Piecewise polynomial reconstructions are, in general, discontinuous at the cell interfaces, $x = x_{j+\frac{1}{2}}$, and therefore their evolution is locally described by the solutions of generalized Riemann problems. The sizes of the corresponding Riemann fans are determined by the right- and left-sided local speeds of propagation, $\{a^{\pm}_{j+\frac{1}{2}}\}$, which can be estimated as follows:

$$\begin{aligned} a^{+}_{j+\frac{1}{2}} &:= \max_{\boldsymbol{\omega}\in C(\mathbf{u}^{-}_{j+\frac{1}{2}},\mathbf{u}^{+}_{j+\frac{1}{2}})}\left\{\lambda_N\left(\frac{\partial \mathbf{f}}{\partial \mathbf{u}}(\boldsymbol{\omega})\right), 0\right\},\\ a^{-}_{j+\frac{1}{2}} &:= \min_{\boldsymbol{\omega}\in C(\mathbf{u}^{-}_{j+\frac{1}{2}},\mathbf{u}^{+}_{j+\frac{1}{2}})}\left\{\lambda_1\left(\frac{\partial \mathbf{f}}{\partial \mathbf{u}}(\boldsymbol{\omega})\right), 0\right\}. \end{aligned} \tag{2.2}$$

Here, $\lambda_1 < \cdots < \lambda_N$ are the eigenvalues of the Jacobian $\frac{\partial \mathbf{f}}{\partial \mathbf{u}}$, and $C(\mathbf{u}^{-}_{j+\frac{1}{2}}, u^{+}_{j+\frac{1}{2}})$ is the curve in the phase space that connects the left and right values of the reconstruction at $x = x_{j+\frac{1}{2}}$:

$$\mathbf{u}^{-}_{j+\frac{1}{2}} := \mathbf{p}_j(x_{j+\frac{1}{2}}), \quad \mathbf{u}^{+}_{j+\frac{1}{2}} := \mathbf{p}_{j+1}(x_{j+\frac{1}{2}}). \tag{2.3}$$

The cell averages $\{\bar{\mathbf{u}}_j\}$ are then evolved in time according to the semidiscrete central-upwind scheme:

$$\frac{d}{dt}\bar{\mathbf{u}}_j(t) = -\frac{\mathbf{H}_{j+\frac{1}{2}}(t) - \mathbf{H}_{j-\frac{1}{2}}(t)}{\Delta x}, \tag{2.4}$$

where the numerical fluxes $\mathbf{H}_{j+\frac{1}{2}}$ are

$$\mathbf{H}_{j+\frac{1}{2}}(t) = \frac{a^+_{j+\frac{1}{2}}\mathbf{f}(\mathbf{u}^-_{j+\frac{1}{2}}) - a^-_{j+\frac{1}{2}}\mathbf{f}(\mathbf{u}^+_{j+\frac{1}{2}})}{a^+_{j+\frac{1}{2}} - a^-_{j+\frac{1}{2}}} + \frac{a^+_{j+\frac{1}{2}}a^-_{j+\frac{1}{2}}}{a^+_{j+\frac{1}{2}} - a^-_{j+\frac{1}{2}}}\left[\mathbf{u}^+_{j+\frac{1}{2}} - \mathbf{u}^-_{j+\frac{1}{2}}\right]. \tag{2.5}$$

Notice that a practical implementation of (2.4)–(2.5) requires the following:

(i) A stable, preferably a strong stability preserving (SSP) [7], solver for the ODE system (2.4). In all numerical experiments presented below, we have used the third-order SSP Runge–Kutta method. To guarantee that no wave interaction occurs during each time step, the CFL number has been set to 0.5.

(ii) A choice of a piecewise polynomial reconstruction (see the discussion in section 3). Notice that the spatial order of the resulting scheme is determined by the order of the reconstruction.

(iii) A practical version of formula (2.2) for computing the one-sided local speeds of propagation. It is well known that in the convex case, they can be computed by

$$\begin{aligned} a^+_{j+\frac{1}{2}} &= \max\left\{\lambda_N\left(\frac{\partial\mathbf{f}}{\partial\mathbf{u}}(\mathbf{u}^-_{j+\frac{1}{2}})\right), \lambda_N\left(\frac{\partial\mathbf{f}}{\partial\mathbf{u}}(\mathbf{u}^+_{j+\frac{1}{2}})\right), 0\right\},\\ a^-_{j+\frac{1}{2}} &= \min\left\{\lambda_1\left(\frac{\partial\mathbf{f}}{\partial\mathbf{u}}(\mathbf{u}^-_{j+\frac{1}{2}})\right), \lambda_1\left(\frac{\partial\mathbf{f}}{\partial\mathbf{u}}(\mathbf{u}^+_{j+\frac{1}{2}})\right), 0\right\}. \end{aligned} \tag{2.6}$$

In the nonconvex case, however, this simple formula is incorrect if the flux convexity changes near $\mathbf{u}^\pm_{j+\frac{1}{2}}$, and one has to use a more accurate estimate of $a^\pm_{j+\frac{1}{2}}$ there.

In the scalar case, the speeds in (2.2) can be easily evaluated exactly:

$$a^+_{j+\frac{1}{2}} = \max_{u\in[u^{\min}_{j+\frac{1}{2}}, u^{\max}_{j+\frac{1}{2}}]}\{f'(u), 0\}, \quad a^-_{j+\frac{1}{2}} = \min_{u\in[u^{\min}_{j+\frac{1}{2}}, u^{\max}_{j+\frac{1}{2}}]}\{f'(u), 0\},$$

where $u^{\min}_{j+\frac{1}{2}} = \min\{u^-_{j+\frac{1}{2}}, u^+_{j+\frac{1}{2}}\}$ and $u^{\max}_{j+\frac{1}{2}} = \max\{u^-_{j+\frac{1}{2}}, u^+_{j+\frac{1}{2}}\}$.

In the case of a system, we follow the approach in [37] if the structure coefficients,

$$\kappa_i = \nabla_{\mathbf{u}}\lambda_i \cdot \mathbf{r}_i, \quad i = 1, \ldots, N, \tag{2.7}$$

change sign near $\mathbf{u}^\pm_{j+\frac{1}{2}}$ (here $\mathbf{r}_i$ is the ith right eigenvector, corresponding to the ith eigenvalue λ_i). The left and right local speeds are then estimated by

$$\begin{aligned} a^+_{j+\frac{1}{2}} &= \max\left\{\lambda_N\left(\frac{\partial\mathbf{f}}{\partial\mathbf{u}}(\mathbf{u}^-_{j+\frac{1}{2}})\right), \lambda_N\left(\frac{\partial\mathbf{f}}{\partial\mathbf{u}}(\mathbf{u}^+_{j+\frac{1}{2}})\right), \widetilde{\mathcal{H}}_N, 0\right\},\\ a^-_{j+\frac{1}{2}} &= \min\left\{\lambda_1\left(\frac{\partial\mathbf{f}}{\partial\mathbf{u}}(\mathbf{u}^-_{j+\frac{1}{2}})\right), \lambda_1\left(\frac{\partial\mathbf{f}}{\partial\mathbf{u}}(\mathbf{u}^+_{j+\frac{1}{2}})\right), \widetilde{\mathcal{H}}_1, 0\right\}. \end{aligned} \tag{2.8}$$

Here, the notation is

$$\widetilde{\mathcal{H}}_N := \max_{\sigma\in[0,1]} \mathcal{H}(\lambda_N(\mathbf{u}^-_{j+\frac12}), \lambda_N(\mathbf{u}^+_{j+\frac12}), \kappa^-_N, \kappa^+_N; \sigma),$$

$$\widetilde{\mathcal{H}}_1 := \min_{\sigma\in[0,1]} \mathcal{H}(\lambda_1(\mathbf{u}^-_{j+\frac12}), \lambda_1(\mathbf{u}^+_{j+\frac12}), \kappa^-_1, \kappa^+_1; \sigma),$$

where

$$\kappa^\pm_i := \nabla_{\mathbf{u}}\lambda_i(\mathbf{u}^\pm_{j+\frac12}) \cdot \mathbf{r}_i(\mathbf{u}^{\text{mid}}_{j+\frac12}), \quad \mathbf{u}^{\text{mid}}_{j+\frac12} = \frac{\mathbf{u}^+_{j+\frac12} + \mathbf{u}^-_{j+\frac12}}{2}, \qquad i = 1, N, \tag{2.9}$$

are the left and right structure coefficients at $x_{j+\frac12}$, and $\mathcal{H}(a, b, a', b'; \sigma)$ is the unique Hermite cubic polynomial that satisfies the following interpolation conditions:

$$\mathcal{H}(a, b, a', b'; 0) = a, \;\; \mathcal{H}(a, b, a', b'; 1) = b, \;\; \mathcal{H}'(a, b, a', b'; 0) = a', \;\; \mathcal{H}'(a, b, a', b'; 1) = b'.$$

Away from the regions where the convexity changes, the local speeds are computed by (2.6).

Remark. In the 2-D case, we use a higher-order version of the central-upwind scheme from [15], where a fourth-order central-upwind numerical flux was obtained. Proceeding along the lines of the numerical flux derivation in [15] and replacing Simpson's rule with the 3-point Gaussian quadrature in the evaluation of the spatial flux integrals, we arrive at the following semidiscrete central-upwind scheme:

$$\frac{d}{dt}\bar{\mathbf{u}}_{j,k}(t) = -\frac{\mathbf{H}^x_{j+\frac12,k}(t) - \mathbf{H}^x_{j-\frac12,k}(t)}{\Delta x} - \frac{\mathbf{H}^y_{j,k+\frac12}(t) - \mathbf{H}^y_{j,k-\frac12}(t)}{\Delta y}, \tag{2.10}$$

where the numerical fluxes are

(2.11)

$$\begin{aligned}
\mathbf{H}^x_{j+\frac12,k} := {} & \frac{a^+_{j+\frac12,k}}{18(a^+_{j+\frac12,k} - a^-_{j+\frac12,k})}\Big[5\mathbf{f}(\mathbf{u}^{\text{E1}}_{j,k}) + 8\mathbf{f}(\mathbf{u}^{\text{E2}}_{j,k}) + 5\mathbf{f}(\mathbf{u}^{\text{E3}}_{j,k})\Big] \\
& - \frac{a^-_{j+\frac12,k}}{18(a^+_{j+\frac12,k} - a^-_{j+\frac12,k})}\Big[5\mathbf{f}(\mathbf{u}^{\text{W1}}_{j+1,k}) + 8\mathbf{f}(\mathbf{u}^{\text{W2}}_{j+1,k}) + 5\mathbf{f}(\mathbf{u}^{\text{W3}}_{j+1,k})\Big] \\
& + \frac{a^+_{j+\frac12,k}a^-_{j+\frac12,k}}{18(a^+_{j+\frac12,k} - a^-_{j+\frac12,k})} \\
& \times \Big[5(\mathbf{u}^{\text{W1}}_{j+1,k} - \mathbf{u}^{\text{E1}}_{j,k}) + 8(\mathbf{u}^{\text{W2}}_{j+1,k} - \mathbf{u}^{\text{E2}}_{j,k}) + 5(\mathbf{u}^{\text{W3}}_{j+1,k} - \mathbf{u}^{\text{E3}}_{j,k})\Big]
\end{aligned}$$

and

(2.12)

$$\begin{aligned}
\mathbf{H}^y_{j,k+\frac12} := {} & \frac{b^+_{j,k+\frac12}}{18(b^+_{j,k+\frac12} - b^-_{j,k+\frac12})}\Big[5\mathbf{g}(\mathbf{u}^{\text{N1}}_{j,k}) + 8\mathbf{g}(\mathbf{u}^{\text{N2}}_{j,k}) + 5\mathbf{g}(\mathbf{u}^{\text{N3}}_{j,k})\Big] \\
& - \frac{b^-_{j,k+\frac12}}{18(b^+_{j,k+\frac12} - b^-_{j,k+\frac12})}\Big[5\mathbf{g}(\mathbf{u}^{\text{S1}}_{j,k+1}) + 8\mathbf{g}(\mathbf{u}^{\text{S2}}_{j,k+1}) + 5\mathbf{g}(\mathbf{u}^{\text{S3}}_{j,k+1})\Big]
\end{aligned}$$

$$+\frac{b^+_{j,k+\frac12}b^-_{j,k+\frac12}}{18(b^+_{j,k+\frac12}-b^-_{j,k+\frac12})}$$

$$\times\Big[5(\mathbf{u}^{\mathrm{S}1}_{j,k+1}-\mathbf{u}^{\mathrm{N}1}_{j,k})+8(\mathbf{u}^{\mathrm{S}2}_{j,k+1}-\mathbf{u}^{\mathrm{N}2}_{j,k})+5(\mathbf{u}^{\mathrm{S}3}_{j,k+1}-\mathbf{u}^{\mathrm{N}3}_{j,k})\Big].$$

Here, the Cartesian grid is assumed to be uniform with $x_\alpha=\alpha\Delta x$, $y_\beta=\beta\Delta y$; the point values $\mathbf{u}^{\mathrm{E}i}_{j,k}$, $i=1,2,3$, are the values of the polynomial piece over the cell $[x_{j-\frac12},x_{j+\frac12}]\times[y_{k-\frac12},y_{k+\frac12}]$, evaluated at the corresponding Gaussian nodes along the eastern edge ($x=x_{j+\frac12}$, $y_{k-\frac12}<y<y_{k+\frac12}$); the point values $\mathbf{u}^{\mathrm{N}i}_{j,k}$, $i=1,2,3$, are the values of the polynomial piece over the same cell evaluated at the corresponding Gaussian nodes along the northern edge ($x_{j-\frac12}<x<x_{j+\frac12}$, $y=y_{k+\frac12}$); and the rest of the point values, $\mathbf{u}^{\mathrm{W}i}_{j,k}$, $\mathbf{u}^{\mathrm{S}i}_{j,k}$, $i=1,2,3$, are calculated at the Gaussian nodes along the remaining two edges. Recall that the Gaussian nodes G_i, $i=1,2,3$, on an arbitrary segment AB with $A=(a_1,a_2)$ and $B=(b_1,b_2)$ have the following coordinates: $G_1=(\alpha_+a_1+\alpha_-a_2,\alpha_+b_1+\alpha_-b_2)$, $G_2=((a_1+a_2)/2,(b_1+b_2)/2)$, and $G_3=(\alpha_-a_1+\alpha_+a_2,\alpha_-b_1+\alpha_+b_2)$, where $\alpha_\pm=\frac12(1\pm\sqrt{3/5})$.

The local speeds of propagation in the x- and y-direction, $a^\pm_{j+\frac12,k}$ and $b^\pm_{j,k+\frac12}$, respectively, are computed at the midpoint of each cell interface in a dimension-by-dimension manner according to the above 1-D recipe.

If the point values in (2.11)–(2.12) are computed using an rth-order piecewise polynomial reconstruction, the resulting spatial order of the semidiscrete central-upwind scheme (2.10)–(2.12) will be $\min(r,6)$ due to the accuracy limitation of the Gaussian formula. When a second-order piecewise linear reconstruction is utilized, the sixth-order fluxes (2.11)–(2.12) can be replaced by their simpler second-order versions (see, e.g., [15], [17]).

3. Piecewise polynomial reconstructions. In this section, we discuss the effect of different piecewise polynomial reconstructions on the numerical solution, computed by the central-upwind schemes. We will consider several second-order reconstructions and the fifth-order WENO5 reconstruction, each of which will be applied to the conservative variables componentwise (therefore, all the variables used in this section are scalar). In the nonconvex case, the choice of reconstruction is particularly important for computing the unique entropy solution, especially when composite waves are present.

In general, in order to achieve high resolution, the piecewise polynomial reconstruction should be of an appropriate order of accuracy and nonoscillatory. For second-order piecewise linear reconstructions (see (2.1)), the first requirement can be easily achieved by ensuring $s_j=u_x(x_j,t)+\mathcal{O}(\Delta x)$, while to satisfy the nonoscillatory property, the reconstruction has to utilize a nonlinear limiter. A library of such reconstructions is available (see, e.g., [35], [19], [8], [22], [28], [30], [34]). In the numerical experiments, reported in section 5, we have tested several well-known limiters, such as the generalized minmod limiter ([8], [22], [28], [34]),

$$s_j=\mathrm{minmod}\left(\theta\frac{\bar u_j-\bar u_{j-1}}{\Delta x},\ \frac{\bar u_{j+1}-\bar u_{j-1}}{2\Delta x},\ \theta\frac{\bar u_{j+1}-\bar u_j}{\Delta x}\right),\quad \theta\in[1,2], \tag{3.1}$$

where the minmod function is defined by

$$\text{minmod}(z_1, z_2, \ldots) := \begin{cases} \min_j\{z_j\} & \text{if } \ z_j > 0 \ \ \forall j, \\ \max_j\{z_j\} & \text{if } \ z_j < 0 \ \ \forall j, \\ 0 & \text{otherwise,} \end{cases}$$

and the superbee limiter ([19], [22], [30], [34]),

$$s_j = \frac{\bar{u}_j - \bar{u}_{j-1}}{\Delta x} \max\left\{0, \min(2r, 1), \min(r, 2)\right\}, \quad r = \frac{\bar{u}_{j+1} - \bar{u}_j}{\bar{u}_j - \bar{u}_{j-1}}. \tag{3.2}$$

Note that the generalized minmod limiter (3.1) with $\theta = 1$ reduces to the standard (dissipative) minmod limiter, which will be referred to as the MM1 limiter. The other limiting case ($\theta = 2$) corresponds to the most compressive minmod limiter, which from now on, will be denoted by MM2. The superbee limiter will be denoted by SB.

In many cases, especially when smooth parts of the solution have a complicated structure, it may be advantageous to use higher (than second)-order reconstructions. We refer the reader to [3], [16], [19], [20], [21], [25] for numerous examples of higher-order reconstructions. A very popular family of such reconstructions are the so-called WENO reconstructions. They were first introduced in [26] and since have been extended to higher orders, multiple numbers of dimensions, and finite-difference setting (see, e.g., [3], [12], [32], [33] and the references therein). In our numerical experiments, we have used the fifth-order finite-volume WENO5 reconstruction, applied componentwise and extended to the 2-D case in a dimension-by-dimension manner as described in [32].

In practice, the reconstruction selection depends on the problem at hand. When the entropy solution does not admit composite waves, the implementation of a compressive second-order reconstruction or a higher-order one typically results in a high quality numerical solution, since both smooth and discontinuous (shocks, contacts) parts of the solution are approximated more accurately than by a more dissipative reconstruction, such as the MM1 one. However, the situation is more complicated in the nonconvex case, in which a formation of composite waves is possible. This problem is best understood in the case of a 1-D scalar equation, which is the simplest conservation law whose solutions admit composite waves.

3.1. One-dimensional scalar conservation laws. Composite waves (see [19]) consist of a sequence of joined rarefactions and shocks. A generic case is a shock adjacent to a rarefaction wave, in the computation of which the reconstruction selection seems to be crucial. As we illustrate below, a numerical scheme that uses the generalized minmod limiter (3.1) with $\theta > 1$ or even the more compressive SB may result in capturing a numerical solution that converges to a weak solution, consisting of a shock, adjacent to an artificial constant state, followed by a rarefaction wave. Moreover, the rarefaction may be completely missing (see Figure 3.4), and the shock location and strength may be totally different from those in the unique entropy solution.

We now consider a particular example: a Riemann problem for the 1-D scalar equation

$$u_t + f(u)_x = 0 \tag{3.3}$$

with the C^1 monotone increasing flux, whose convexity changes at $u = 1/2$:

$$f(u) = \begin{cases} \dfrac{u(1-u)}{4}, & u < \dfrac{1}{2}, \\ \dfrac{1}{2}u^2 - \dfrac{1}{2}u + \dfrac{3}{16}, & u \geq \dfrac{1}{2}. \end{cases} \tag{3.4}$$

While the Kruzhkov entropy solution can be easily obtained for any (nonconvex) smooth flux function (see, e.g., [18]), numerically solving (3.3) by a high-order scheme may be quite a challenging problem.

We apply the central-upwind semidiscretization (2.2)–(2.5) to (3.3)–(3.4). Due to the monotonicity of the flux (3.4), $a^-_{j+\frac{1}{2}} = 0$, and thus the central-upwind scheme (2.2)–(2.5) reduces to a simple semidiscrete upwinding:

$$\frac{d}{dt}\bar{u}_j(t) = -\frac{f(u^-_{j+\frac{1}{2}}) - f(u^-_{j-\frac{1}{2}})}{\Delta x}. \tag{3.5}$$

We first solve (3.3)–(3.4) subject to the initial condition:

$$u(x,0) = \begin{cases} 0, & x < 0.25, \\ 1, & 0.25 < x. \end{cases} \tag{3.6}$$

In Figure 3.1, we show the solutions computed at time $t = 1$ on a uniform grid with $\Delta x = 1/1600$ using the second-order upwind scheme (3.5), (2.1), (2.3) with compressive MM2 and SB reconstructions. One can clearly see that in both cases, the captured solution is not the Kruzhkov entropy solution, which consists of a shock, located at $x = (\sqrt{6}-1)/4$, followed by a rarefaction wave. Moreover, we have performed a numerical convergence study which clearly indicates that both numerical approximations fail to converge to the entropy solution.

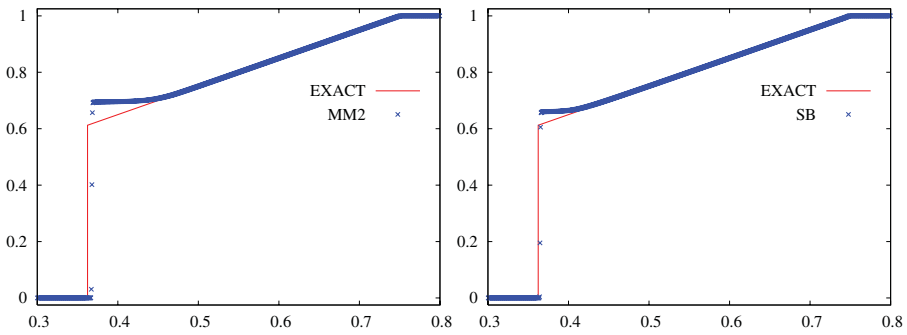

FIG. 3.1. *Solutions of* (3.3)–(3.4), (3.6) *computed with MM2 (left) and SB (right).*

At the same time, we observe that the same method, but with the dissipative MM1 reconstruction, leads to the convergence of the computed solutions toward the unique entropy solution; see Figure 3.2 (left) and Figure 3.2 (right), where a mesh refinement study is performed.

In this example, the evolution step is performed using the semidiscrete upwind scheme (3.5), (2.1), (2.3) and the third-order SSP Runge–Kutta ODE solver. A natural question to ask is whether the observed effect is due to the particular spatial

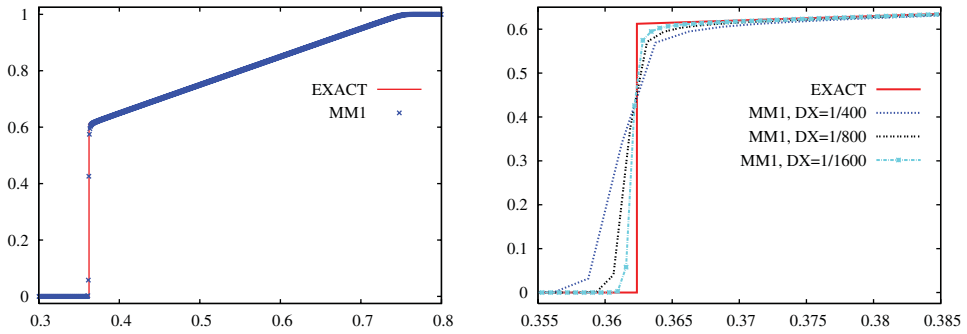

FIG. 3.2. *Solutions of* (3.3)–(3.4), (3.6) *computed with MM*1 *(left) and its convergence test (right, zoom at the composite wave area).*

discretization and time integration used or is a consequence of the implemented reconstruction. It turns out that if we start with a compressive piecewise linear reconstruction at time $t = t^n$ and evolve it exactly to the next time level $t = t^{n+1}$, according to the integral formulation of (3.3),

(3.7)
$$\bar{u}_j(t^{n+1}) = \bar{u}_j(t^n) - \frac{1}{\Delta x}\left[\int_{t^n}^{t^{n+1}} f(u(x_{j+\frac{1}{2}},\tau))\,d\tau - \int_{t^n}^{t^{n+1}} f(u(x_{j-\frac{1}{2}},\tau))\,d\tau\right],$$

the same behavior persists. Here, we only need to exactly compute the temporal integrals in (3.7), which can be done analytically when $\Delta t \le 0.5\Delta x$, since the formulae for both the flux function and the exact solution are available (we have taken $\Delta t = 0.5\Delta x$, but smaller time steps lead to the same results).

Snapshots at times $t = 0.1, 0.2, \ldots, 1.0$ of the exactly evolved solutions of the IVP (3.3)–(3.4), (3.6) are presented in Figure 3.3, where the MM1 and MM2 reconstructions are used. In the case of the MM2 reconstruction, the wrong shock location as well as the formation of an artificial constant state between the shock and the rarefaction wave can be clearly seen, while the MM1 solution accurately approximates the composite wave.

Here, the implementation of the MM2 reconstruction (or another compressive reconstruction, for example, the generalized minmod with any $\theta > 1$ or the SB) leads to an initial overshoot in a single cell—the last cell with a cell-average value less than 1. As time progresses, the overshoot persists and, because of the error propagation, spreads over neighboring cells. At the same time, the moving shock cannot balance the effect of the overshoot, because (i) the overshoot speed is higher than the shock speed, and (ii) the large jumps from the shock feed the overshoot and thus oppose its smearing by the rarefication process and the numerical diffusion. As a result, an artificial constant state between the shock and rarefaction wave is formed. In the case of a generalized minmod reconstruction, its value depends on the value of θ and the size of the initial shock.

The above problem seems to get resolved if we use the dissipative MM1 reconstruction. The successful resolution of composite waves in this case is due to the fact that the smaller of the jumps, $\bar{u}_{j+1} - \bar{u}_j$ or $\bar{u}_j - \bar{u}_{j-1}$, is used to determine the corresponding slope s_j in (2.1). The calculation of the new local cell averages over/near the border between the shock and rarefaction is mostly based on the information from

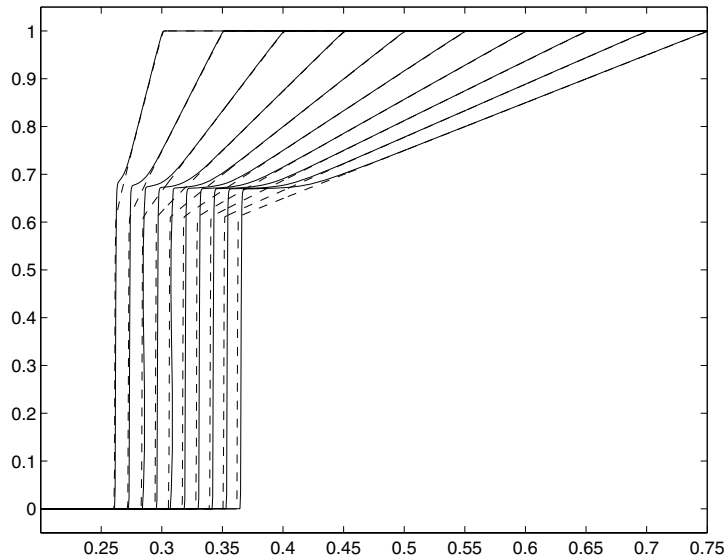

FIG. 3.3. *Exact evolution of the MM*1 *and MM*2 *reconstructions;* $\Delta x = 1/2000$.

the rarefaction part of the computed solution (where the jumps are smaller), and thus the shock impact on the evaluation of these averages is substantially reduced.

So far, the discussion has been restricted to second-order piecewise linear reconstructions since in this case one can relatively easily understand the effects of different reconstructions on the computed solutions. The situation gets much more complicated when a higher-order (for example, the fifth-order WENO5) reconstruction is employed. In the scalar 1-D case, we were unable to find an example in which the WENO5 reconstruction leads to capturing a non-Kruzhkov weak solution. However, our example of a 1-D system (section 5.2) and the 2-D scalar example (section 5.3) clearly illustrate that the WENO5-based scheme may fail to resolve composite waves; see Figures 5.4, 5.7, and 5.10, respectively.

We conclude this section with yet another numerical example, which illustrates that if a compressive reconstruction is employed, a rarefaction part of the composite wave can be completely missed, while the use of the dissipative MM1 reconstruction leads to capturing the unique entropy solution. We compute the solution of the same equation (3.3)–(3.4) subject to different initial data:

$$u(x,0) = \begin{cases} 1, & x < 0.25, \\ 0, & 0.25 < x. \end{cases} \tag{3.8}$$

In Figure 3.4, we show the solutions computed at time $t = 2$ on a uniform grid with $\Delta x = 1/1600$ using the second-order upwind scheme (3.5), (2.1), (2.3) with compressive MM2 and SB reconstructions. One can clearly see that in both cases, the captured solution is a simple shock wave—not the Kruzhkov entropy solution, which consists of a shock, located at $x = (2\sqrt{3}-1)/4$, followed by a rarefaction wave. In Figure 3.5, we present the solution, computed by the same method but with the dissipative MM1 reconstruction. As in the previous example, one can observe the convergence of the numerical solutions toward the unique entropy solution.

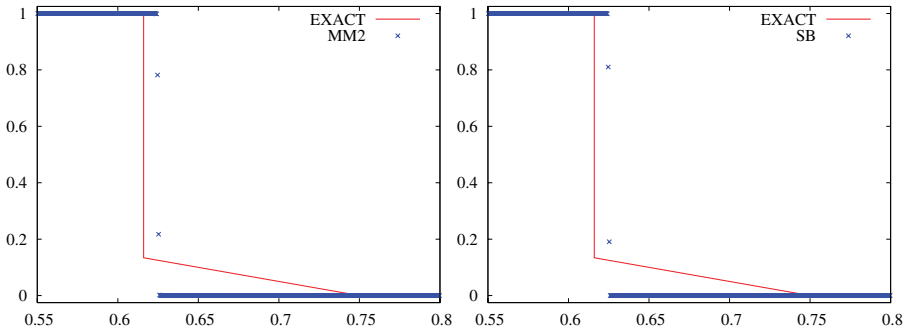

FIG. 3.4. *Solutions of* (3.3)–(3.4), (3.8) *computed with MM*2 *(left) and SB (right).*

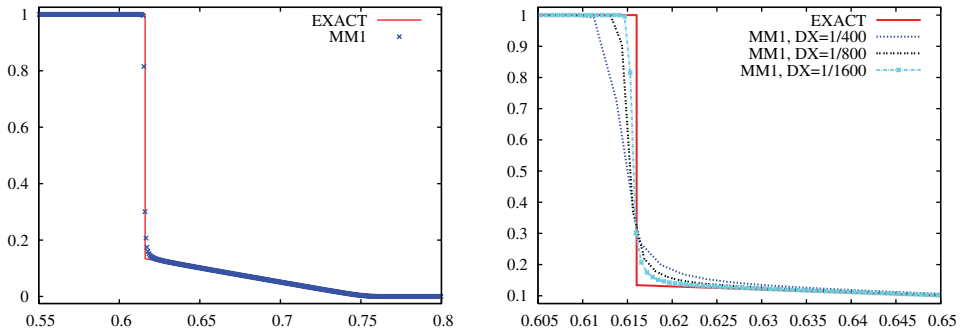

FIG. 3.5. *Solutions of* (3.3)–(3.4), (3.8) *computed with MM*1 *(left) and its convergence test (right, zoom at the composite wave area).*

4. Scheme adaption algorithm. It is a well-known fact that more compressive second-order and/or higher-order piecewise polynomial reconstructions typically lead to a higher resolution than the one that can be achieved with the help of the dissipative MM1 reconstruction. However, as observed in the previous section, the use of higher resolution reconstructions may be dangerous at the presence of composite waves, while the use of the MM1 reconstruction seems to ensure the convergence toward these waves.

We now describe a simple adaption strategy that will utilize the advantages of higher resolution reconstructions away from the composite waves, which, in turn, will be locally approximated using the MM1 reconstruction.

- Use the MM1 reconstruction only in the transition zones—in a small number of cells around points where the flux convexity changes (that is, where f'' or one of the κ_i's in (2.9) changes sign).
- Use a higher resolution reconstruction otherwise.

Remarks.

1. In all numerical experiments presented below, we have used the finite-volume WENO5 reconstruction—applied componentwise to the 1-D systems and in a dimension-by-dimension manner in the 2-D case—as a higher resolution component of our adaptive algorithm.
2. Our extensive numerical experiments suggest that in order to ensure convergence to the unique entropy solution, the number of cells where the MM1

reconstruction is used should be relatively small and could be taken proportional to $|\ln(\Delta x)|$ as the grid is refined.

5. Numerical examples. In this section, we numerically solve nonconvex 1-D hyperbolic systems of conservation laws and a 2-D scalar conservation law with nonconvex fluxes. We apply the semidiscrete central-upwind schemes described in section 2 with different piecewise polynomial reconstructions including the adaptive reconstruction proposed in section 4.

5.1. One-dimensional Euler equations of gas dynamics. We consider the 1-D Euler equations of gas dynamics,

$$\frac{\partial}{\partial t}\begin{bmatrix}\rho\\ m\\ E\end{bmatrix}+\frac{\partial}{\partial x}\begin{bmatrix}m\\ \rho u^2+p\\ u(E+p)\end{bmatrix}=0, \tag{5.1}$$

with the following nonconvex EOS (see [37]):

$$p=p(\rho,e)=((\gamma-1)\rho+f(\rho))e,\quad e=\frac{E}{\rho}-\frac{1}{2}u^2,\quad \gamma=1.4, \tag{5.2}$$

where the function f is given by

$$f(\rho)=\begin{cases}10\exp\left(\dfrac{\rho^2}{1-2\rho+0.75\rho^2}\right), & \dfrac{2}{3}<\rho<2,\\ 0 & \text{otherwise,}\end{cases} \tag{5.3}$$

and ρ, u, $m=\rho u$, p, and E are the density, velocity, momentum, pressure, and total energy, respectively. It can be shown that system (5.1) with the EOS given by (5.2)–(5.3) is hyperbolic.

The computation of the numerical solution of (5.1)–(5.3), using the scheme (2.4)–(2.5), (2.3), (2.8), combined with different piecewise polynomial reconstructions requires the calculation of the one-sided local speeds of propagation, and therefore the computation of the corresponding structure coefficients (2.9). Here, we have

$$\kappa_1^{\pm}=\left(-\frac{m^{\pm}}{(\rho^{\pm})^2}-c_\rho^{\pm}\right)+\left(\frac{1}{\rho^{\pm}}-c_m^{\pm}\right)(u_{mid}-c_{mid})-c_E^{\pm}\left(\frac{E_{mid}+p_{mid}}{\rho_{mid}}-u_{mid}c_{mid}\right),$$

$$\kappa_3^{\pm}=\left(-\frac{m^{\pm}}{(\rho^{\pm})^2}+c_\rho^{\pm}\right)+\left(\frac{1}{\rho^{\pm}}+c_m^{\pm}\right)(u_{mid}+c_{mid})+c_E^{\pm}\left(\frac{E_{mid}+p_{mid}}{\rho_{mid}}+u_{mid}c_{mid}\right),$$

where c is the sound speed,

$$c^2=p_\rho+\frac{pp_e}{\rho^2},$$

and

$$\mathcal{R}_{mid}:=\frac{\mathcal{R}^+ +\mathcal{R}^-}{2}$$

for $\mathcal{R}$ being ρ, u, c, p, or E. The corresponding partial derivatives are

$$c_m=-\frac{m}{2\rho^2}T,\qquad c_E=\frac{1}{2\rho}T,$$

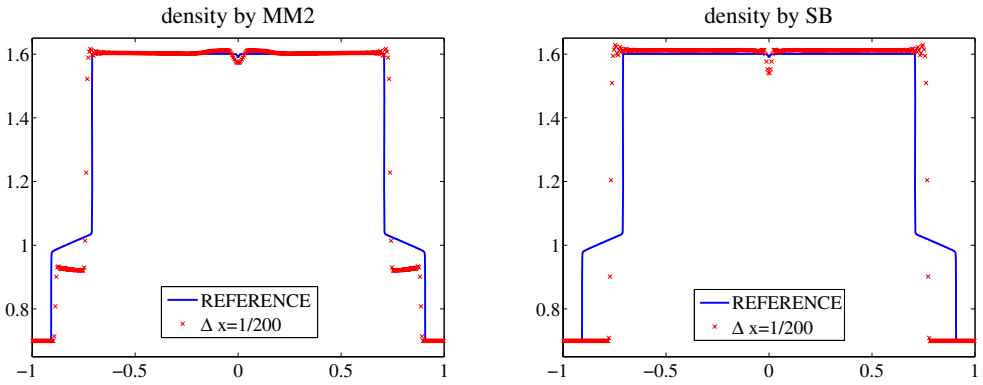

FIG. 5.1. *Solutions of* (5.1)–(5.4), *computed with MM2 (left) and SB (right).*

$$c_\rho = \frac{m^2 - E\rho}{2\rho^3}T + \frac{1}{2T}\left(f''(\rho) + \frac{(0.8\rho + 2f(\rho))(f'(\rho)\rho - f(\rho))}{\rho^3}\right),$$

where

$$T = \left(\frac{0.4 + f'(\rho) + (0.4 + f(\rho)\rho^{-1})^2}{E\rho^{-1} - 0.5m^2\rho^{-2}}\right)^{\frac{1}{2}}.$$

We solve the system (5.1)–(5.3) subject to the initial data (see [37]):

$$(p, \rho, u)_L = (0.5, 0.6998, 1), \quad (p, \rho, u)_R = (0.5, 0.6998, -1), \tag{5.4}$$

using the MM1, MM2, SB, and the adaptive reconstruction proposed in section 4. To apply the adaptive strategy from section 4, we need to know where the structure coefficients change sign, which in this case is the same as checking where $p_{\tau\tau}$, $\tau = \rho^{-1}$, changes sign. In this example, $p_{\tau\tau}$ has two isolated zeros $\tau^* = 1/\rho^* = 0.862$ and $\tau^{**} = 1/\rho^{**} = 1.21$. We perform the adaption in the following way. First, we mark all cell pairs with indexes $j, j+1$, for which either $(\rho_{j+1} - \rho^*)(\rho_j - \rho^*) < 0$ or $(\rho_{j+1} - \rho^{**})(\rho_j - \rho^{**}) < 0$. Then we use the MM1 reconstruction in the marked cells and in the cells located within $K\Delta x$ from them, while the WENO5 reconstruction is used in the rest of the computational domain.

We compare the density profiles of the numerical solutions, calculated at time $t = 1$ on a uniform grid with $\Delta x = 1/200$, with the profile of a reference solution, obtained with the "reliable" MM1 limiter and $\Delta x = 1/5000$. The results are presented in Figures 5.1–5.3, where one can clearly see that the composite waves are incorrectly resolved when a compressive piecewise linear reconstruction (either MM2 or SB) is employed, while the central-upwind scheme based on the dissipative MM1 reconstruction accurately captures their structure. Note that in this example, the use of the higher-order WENO5 reconstruction also leads to capturing the entropy solution (see Figure 5.2 (right)). However, the obtained numerical approximation is quite oscillatory, which, together with the failure of the WENO5-based scheme to resolve composite waves in the examples from sections 5.2 and 5.3, makes one doubt the reliability of a pure WENO5 reconstruction.

The solutions, computed by our adaptive central-upwind scheme, are shown in Figure 5.3. When the adaption constant $K = 1$, the obtained solution is basically

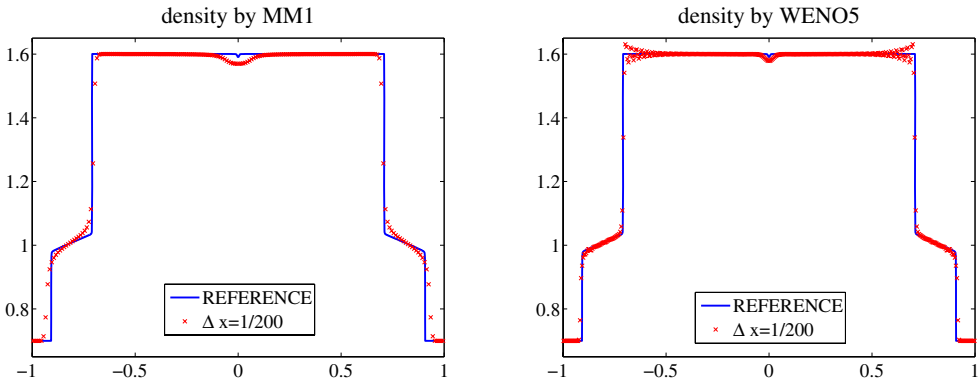

FIG. 5.2. *Solutions of* (5.1)–(5.4), *computed with MM*1 *(left) and WENO*5 *(right).*

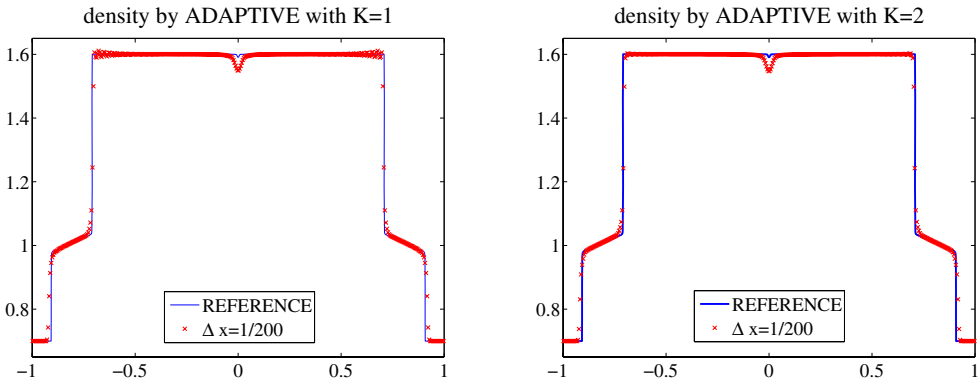

FIG. 5.3. *Solutions of* (5.1)–(5.4), *computed adaptively with* $K = 1$ *(left) and* $K = 2$ *(right).*

as well resolved as that obtained by the WENO5-based scheme, but it still has some oscillations, which are completely removed when a larger ($K = 2$) adaption constant is used. As expected, the adaptive reconstruction offers a better overall resolution of the numerical solution, and thus the adaptive strategy is preferable.

5.2. The polymer system. We consider the 1-D polymer system

$$\frac{\partial}{\partial t}\begin{bmatrix} s \\ b \end{bmatrix} + \frac{\partial}{\partial x}\begin{bmatrix} f(s,c) \\ cf(s,c) \end{bmatrix} = \mathbf{0}, \tag{5.5}$$

where s is the water saturation, c is the polymer concentration in the water, $f(s,c)$ is the fractional flow function of water, $b(s,c) = sc + a(c)$, and $a(c)$ is the adsorption function. Here, we take (see, e.g., [9])

$$f(s,c) = \frac{s^2}{s^2 + (0.5+c)(1-s)^2}, \qquad a(c) = \frac{c}{5(1+c)}. \tag{5.6}$$

Notice that the system (5.5)–(5.6) can be rewritten in the nonconservative form

$$\mathbf{u}_t + A(\mathbf{u})\mathbf{u}_x = \mathbf{0},$$

where $\mathbf{u} = (s, c)^T$ and $A(\mathbf{u})$ has eigenvalues $\lambda_s = f_s(s, c)$ and $\lambda_c = f(s, c)(s + a'(c))^{-1}$ with right eigenvectors $\mathbf{r}_s = (1, 0)^T$, $\mathbf{r}_c = (f_c(s, c), \lambda_c - \lambda_s)^T$ for $s \in (0, 1)$ and $\mathbf{r}_c = (0, 1)^T$ for $s = 0, 1$, respectively. The computation of the one-sided local speeds of propagation (2.8) requires the calculation of the corresponding structure coefficients

$$\kappa_s^{\pm} = f_{ss}(s^{\pm}, c^{\pm}),$$

$$\kappa_c^{\pm} = \frac{f_c^{mid}(f_s^{\pm}(s^{\pm} + a'(c^{\pm})) - f^{\pm})}{(s^{\pm} + a'(c^{\pm}))^2} + \frac{(f^{mid}(s_{mid} + a'(c_{mid}))^{-1} - f_s^{mid})(f_c^{\pm}(s^{\pm} + a'(c^{\pm})) - a''(c^{\pm})f^{\pm})}{(s^{\pm} + a'(c^{\pm}))^2}$$

if $s_{mid} \neq 0, 1$, and

$$\kappa_c^{\pm} = \frac{f_c^{\pm}(s^{\pm} + a'(c^{\pm})) - a''(c^{\pm})f^{\pm}}{(s^{\pm} + a'(c^{\pm}))^2}$$

for $s_{mid} \in \{0, 1\}$. Here, we have used the notation $\mathcal{R}^{mid} := \mathcal{R}(s_{mid}, c_{mid})$, where $s_{mid} := (s^+ + s^-)/2$ and $c_{mid} := (c^+ + c^-)/2$, and $\mathcal{R}^{\pm} := \mathcal{R}(s^{\pm}, c^{\pm})$ for $\mathcal{R}$ being f_s, f_c, or f.

We consider the system (5.5)–(5.6) subject to the Riemann initial data taken from [14]:

$$(s(x, 0), c(x, 0)) = \begin{cases} (0.45, 0), & x \leq 0.252, \\ (0.20, 1), & x > 0.25. \end{cases} \tag{5.7}$$

The exact solution of this IVP is rather complicated and consists of both simple and composite waves (see [13]).

We numerically solve the IVP (5.5)–(5.7) using the central-upwind scheme (2.4)–(2.6), (2.8) with different piecewise polynomial reconstructions of the conserved variables s and b.

For adaption, we check at every grid cell whether a point, where one of the structure coefficients, either

$$\kappa_s = f_{ss}$$

or

$$\kappa_c = \begin{cases} a''f(s + a')^{-3}(f_s(s + a') - f), & 0 < s < 1, \\ (s + a')^{-2}(f_s(s + a') - a''f), & s \in \{0, 1\}, \end{cases}$$

changes sign, is nearby. If this is the case, namely, if the distance between the current grid point and one of the aforementioned points is smaller than $K\Delta x$, then the MM1 reconstruction is used; otherwise the WENO5 reconstruction is used.

In Figure 5.4, we plot the numerical solutions at time $t = 1$, calculated using the MM1 reconstruction with $\Delta x = 1/250$ and $\Delta x = 1/8000$ (the latter is used as a reference solution in all other figures shown in this section).

In Figure 5.5, we compare the c-component of the numerical solutions, computed using the MM1, MM2, SB, and WENO5 reconstructions on three different uniform meshes with $\Delta x = 1/250$, $1/500$, and $1/1000$. As one can clearly see in this figure, only the MM1 numerical solution recovers the correct structure of the composite

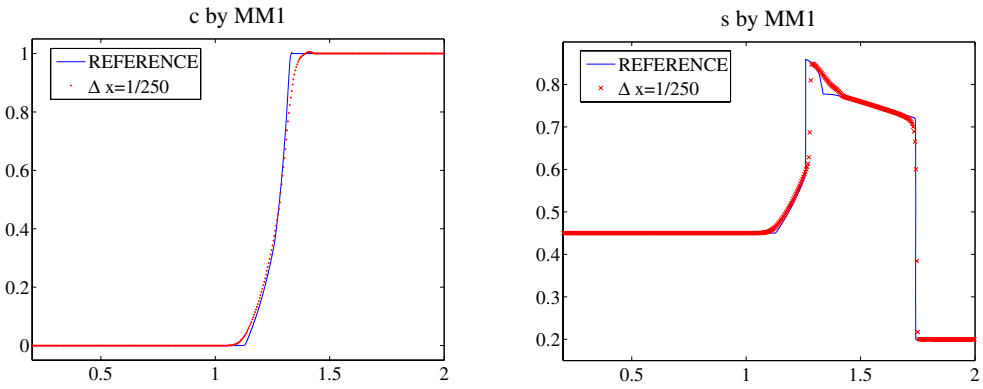

FIG. 5.4. *Solutions of* (5.5)–(5.7), *computed with MM*1*; (left) c- and (right) s-components.*

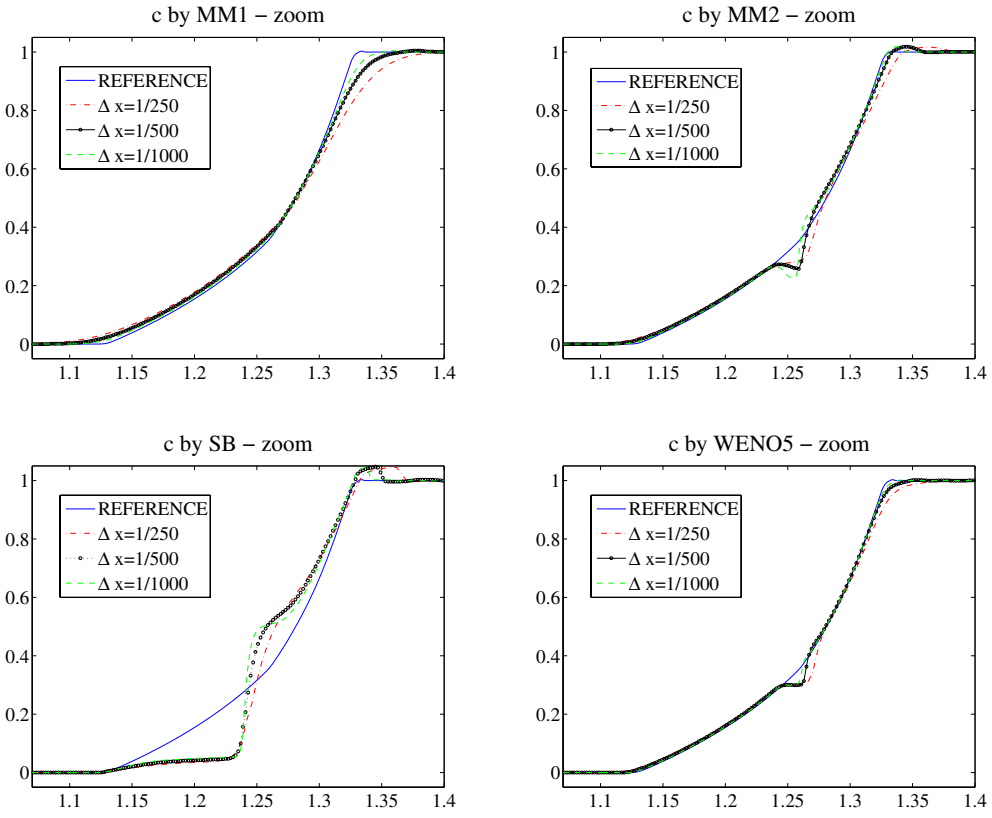

FIG. 5.5. *Solutions (c-component) of* (5.5)–(5.7), *computed with MM*1*, MM*2*, SB, and WENO*5*.*

wave, while the MM2, SB, and WENO5 reconstructions consistently fail to achieve this goal. Note that $\Delta x = 1/1000$ is a reasonably small mesh size that one usually uses in practical computations for such a problem (in the 2-D case, one would have to use an even coarser grid). To perform a numerical convergence study, we have computed the solution with even smaller Δx. It turns out that the numerical approximation

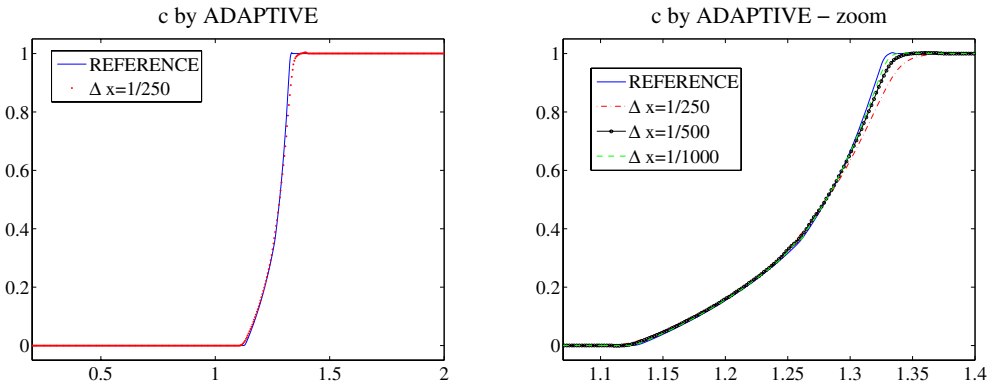

FIG. 5.6. *Solutions (c-component) of* (5.5)–(5.7), *computed adaptively with* $K = 2$ *(left) and its mesh refinement study (right).*

obtained with the WENO5 reconstruction seems to slowly converge to the reference solution, but the values of Δx, required in order to be able to observe this convergence, are so small that this positive result is not of practical interest. On the other hand, the results shown in Figure 5.6 demonstrate that our adaptive strategy both achieves a very high resolution and accurately captures the structure of the composite wave, and thus it is superior to both the lower resolution MM1 solution and the less reliable WENO5 solution.

Next, in Figures 5.7–5.8, we present the s-component of the computed solutions. While the wave structure of the s-component is quite different from that of the c-component, we observe the same effect as before: The central-upwind scheme based on either MM2, SB, or WENO5 reconstruction fails to recover the reference solution even when a very fine mesh with $\Delta x = 1/1000$ is used. At the same time, the schemes based on the MM1 and the adaptive reconstructions perform well. However, as expected, the overall resolution achieved by the adaptive scheme is higher than that achieved by the more dissipative MM1 scheme.

5.3. Two-dimensional scalar conservation law. In this section, we numerically solve the 2-D scalar conservation law

$$u_t + (\sin u)_x + (\cos u)_y = 0, \tag{5.8}$$

subject to the initial data

$$u(x, y, 0) = \begin{cases} 3.5\pi, & x^2 + y^2 < 1, \\ 0.25\pi, & \text{otherwise}, \end{cases} \tag{5.9}$$

using the scheme (2.10)–(2.12) and the piecewise polynomial reconstructions described in sections 3 and 4.

We have computed the solution at time $t = 1$ on a uniform grid with $\Delta x = \Delta y = 1/100$ using the MM1, MM2, SB, WENO5, and the adaptive reconstructions. For adaption, we mark the cells where the convexity of the flux changes, which occurs at $u = k\pi/2$, $k \in \mathbb{Z}$. In these cells and in all cells located within $K \max(\Delta x, \Delta y)$ from them, we use the MM1 reconstruction; otherwise the WENO5 reconstruction is employed.

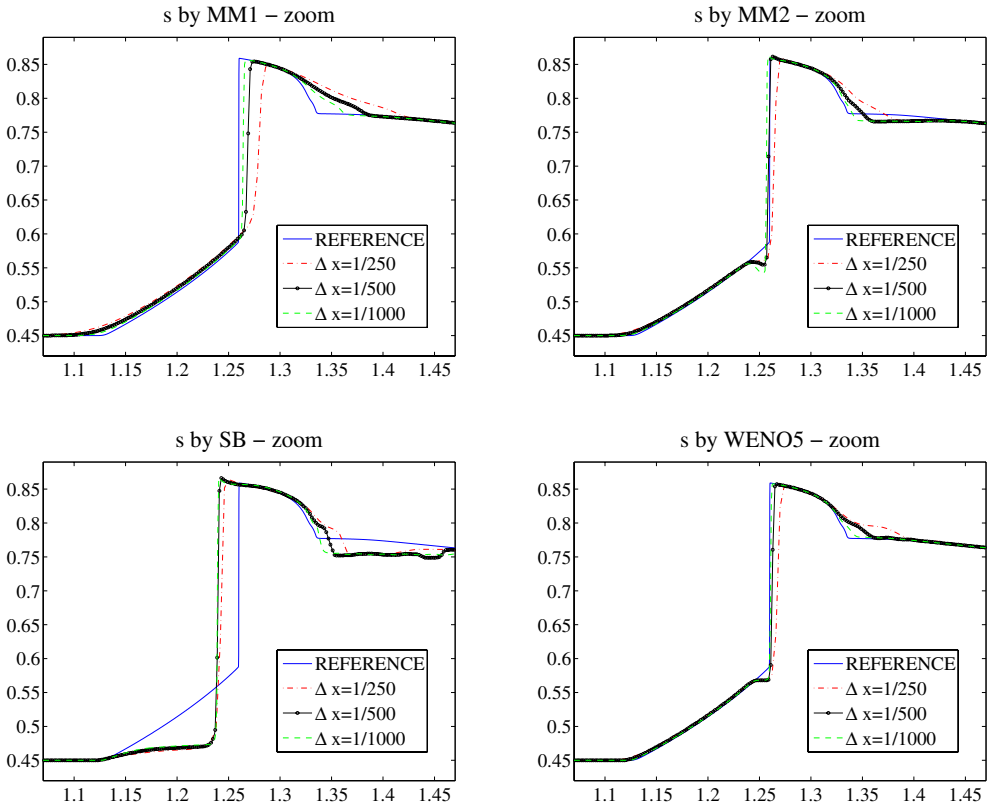

FIG. 5.7. *Solutions (s-component) of* (5.5)–(5.7)*, computed with MM*1*, MM*2*, SB, and WENO*5*.*

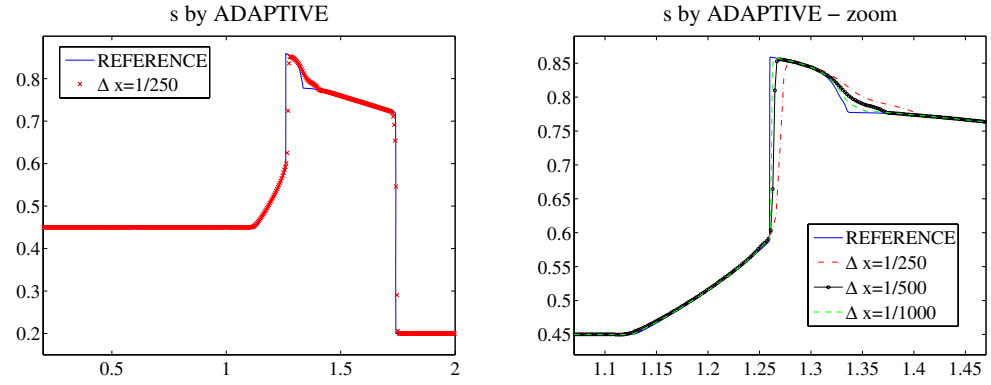

FIG. 5.8. *Solutions (s-component) of* (5.5)–(5.7)*, computed adaptively with* $K = 2$ *(left) and its mesh refinement study (right).*

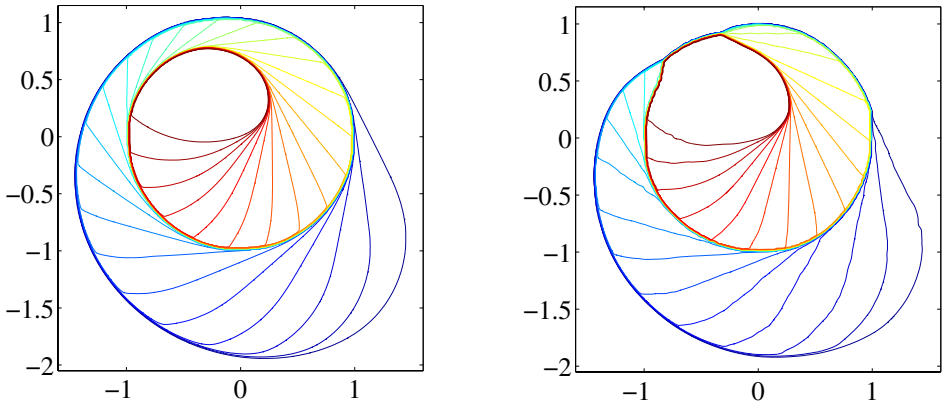

FIG. 5.9. *Solution of* (5.8)–(5.9), *computed with MM*1 *(left) and MM*2 *(right).*

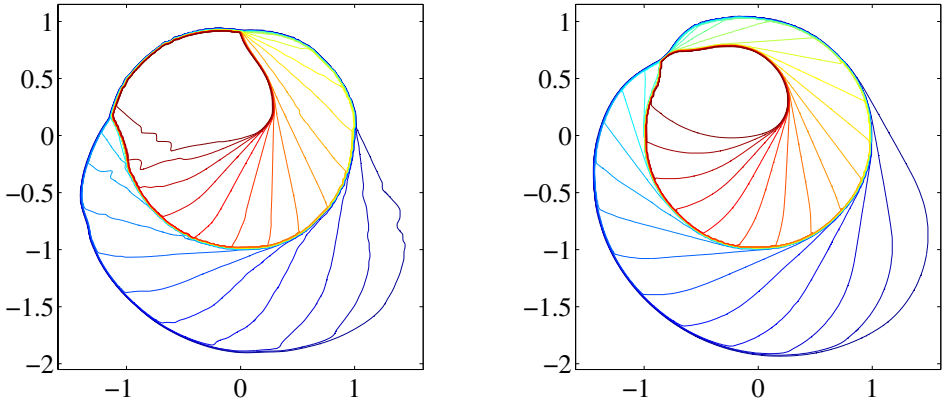

FIG. 5.10. *Solution of* (5.8)–(5.9), *computed with SB (left) and WENO*5 *(right).*

We present our results in Figures 5.9–5.11, where we observe the same effects as in the 1-D case. The central-upwind schemes based on the MM2, SB, and WENO5 reconstructions fail to resolve the composite wave structure, while the use of the MM1 or the adaptive reconstruction leads to capturing the accurate solution. We would like to point out that the adaptive strategy does not seem to be sensitive to the choice of the adaption constant K. We also show (see Figure 5.11 (right)), the areas where the MM1 (white) and the WENO5 (black) reconstructions were used. It can be clearly seen that the MM1 limiter is turned on only at or around transition areas.

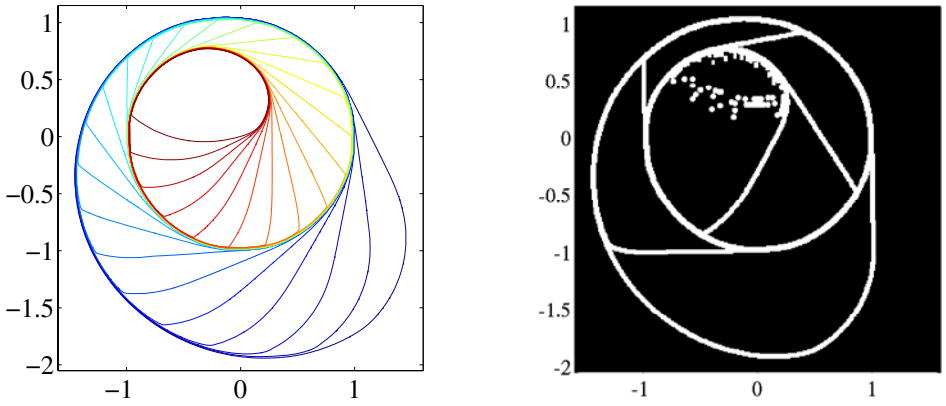

FIG. 5.11. *Solution of* (5.8)–(5.9), *computed adaptively with* $K = 2$ *(left) and the corresponding MM1/WENO5 regions (right).*

Acknowledgments. Part of this work was done in the Fall of 2005, when A. Kurganov visited the Department of Mathematics at the University of Michigan during the semester following Hurricane Katrina. A. Kurganov thanks the chairman, Professor A. Bloch, and all members of the department for their extremely warm hospitality.

REFERENCES

[1] P. BELL, P. COLELLA, AND J. TRANGENSTEIN, *Higher order Godunov methods for general systems of hyperbolic conservation laws*, J. Comput. Phys., 59 (1985), pp. 264–289.
[2] A. BETHE, *Report on the Theory of Shock Waves for an Arbitrary Equation of State*, Technical report PB-32189, U.S. Department of Commerce, 1942.
[3] B. COCKBURN, C. JOHNSON, C.-W. SHU, AND E. TADMOR, *Advanced numerical approximation of nonlinear hyperbolic equations*, CIME Lecture Notes, Lecture Notes in Math. 1697, A. Quarteroni, ed., Springer-Verlag, Berlin, 1997.
[4] P. COLELLA, *Multidimensional upwind methods for hyperbolic conservation laws*, J. Comput. Phys., 87 (1990), pp. 171–200.
[5] P. COLELLA AND H. GLAZ, *Efficient solution algorithms for the Riemann problem for real gases*, J. Comput. Phys., 59 (1985), pp. 264–289.
[6] F. COQUEL AND B. PERTHAME, *Relaxation of energy and approximate Riemann solvers for general pressure laws in fluid dynamics*, SIAM J. Numer. Anal., 35 (1998), pp. 2223–2249.
[7] S. GOTTLIEB, C.-W. SHU, AND E. TADMOR, *Strong stability-preserving high-order time discretization methods*, SIAM Rev., 43 (2001), pp. 89–112.
[8] A. HARTEN AND S. OSHER, *Uniformly high-order accurate nonoscillatory schemes.* I, SIAM J. Numer. Anal., 24 (1987), pp. 279–309.
[9] V. HAUGSE, K. H. KARLSEN, K.-A. LIE, AND J.R. NATVIG, *Numerical solution of the polymer system by front tracking*, Transp. Porous Media, 44 (2001), pp. 63–83.
[10] K. HOLING, J. ALVESTAD, AND J. A. TRANGENSTEIN, *The use of second-order Godunov methods for simulating EOR processes in realistic reservoir models*, in Second European Conference on the Mathematics of Oil Recovery, D. Guérillot and O. Guillon, eds., 1990, pp. 101–111.
[11] E. ISAACSON, *Global Solution of a Riemann Problem for a Non-Strictly Hyperbolic System of Conservation Laws Arising in Enhanced Oil Recovery*, preprint, Rockefeller University, New York, 1981.
[12] G.-S. JIANG AND C.-W. SHU, *Efficient implementation of weighted ENO schemes*, J. Comput. Phys., 126 (1996), pp. 202–228.

[13] T. Johansen and R. Winther, *The solution of the Riemann problem for a hyperbolic system of conservation laws modeling polymer flooding*, SIAM J. Math. Anal., 19 (1988), pp. 541–566.

[14] K. H. Karlsen, K.-A. Lie, J. R. Natvig, H. F. Nordhaug, and H. K. Dahle, *Operator splitting methods for systems of convection-diffusion equations: Nonlinear error mechanisms and correction strategies*, J. Comput. Phys., 173 (2001), pp. 636–663.

[15] A. Kurganov, S. Noelle, and G. Petrova, *Semidiscrete central-upwind schemes for hyperbolic conservation laws and Hamilton–Jacobi equations*, SIAM J. Sci. Comput., 23 (2001), pp. 707–740.

[16] A. Kurganov and G. Petrova, *A third-order semi-discrete genuinely multidimensional central scheme for hyperbolic conservation laws and related problems*, Numer. Math., 88 (2001), pp. 683–729.

[17] A. Kurganov and E. Tadmor, *Solution of two-dimensional Riemann problems for gas dynamics without Riemann problem solvers*, Numer. Methods Partial Differential Equations, 18 (2002), pp. 584–608.

[18] P. G. LeFloch, *Hyperbolic Systems of Conservation Laws. The Theory of Classical and Nonclassical Shock Waves*, Lectures Math. ETH Zürich, Birkhäuser Verlag, Basel, 2002.

[19] R. LeVeque, *Finite Volume Methods for Hyperbolic Problems*, Cambridge Texts Appl. Math., Cambridge University Press, Cambridge, UK, 2002.

[20] D. Levy, G. Puppo, and G. Russo, *Central WENO schemes for hyperbolic systems of conservation laws*, M2AN Math. Model. Numer. Anal., 33 (1999), pp. 547–571.

[21] D. Levy, G. Puppo, and G. Russo, *Compact central WENO schemes for multidimensional conservation laws*, SIAM J. Sci. Comput., 22 (2000), pp. 656–672.

[22] K.-A. Lie and S. Noelle, *On the artificial compression method for second-order nonoscillatory central difference schemes for systems of conservation laws*, SIAM J. Sci. Comput., 24 (2003), pp. 1157–1174.

[23] T.-P. Liu, *The Riemann problem for general* 2×2 *conservation laws*, Trans. Amer. Math. Soc., 199 (1974), pp. 89–112.

[24] T.-P. Liu, *The Riemann problem for general systems of conservation laws*, J. Differential Equations, 18 (1975), pp. 218–234.

[25] X.-D. Liu and S. Osher, *Nonoscillatory high order accurate self-similar maximum principle satisfying shock capturing schemes* I, SIAM J. Numer. Anal., 33 (1996), pp. 760–779.

[26] X.-D. Liu, S. Osher, and T. Chan, *Weighted essentially non-oscillatory schemes*, J. Comput. Phys., 115 (1994), pp. 200–212.

[27] R. Menikoff and B. Plohr, *The Riemann problem for fluid flow of real materials*, Rev. Modern Phys., 61 (1989), pp. 75–130.

[28] H. Nessyahu and E. Tadmor, *Non-oscillatory central differencing for hyperbolic conservation laws*, J. Comput. Phys., 87 (1990), pp. 408–463.

[29] G. A. Pope, *The application of fractional flow theory to enhanced oil recovery*, Soc. Pet. Eng. J., 20 (1980), pp. 191–205.

[30] P. L. Roe, *Characteristic-based schemes for the Euler equations*, in Annual Review of Fluid Mechanics, Vol. 18, Annual Reviews, Palo Alto, CA, 1986, pp. 337–365.

[31] R. Saurel, M. Larini, and J. C. Loraud, *Exact and approximate Riemann solvers for real gases*, J. Comput. Phys., 112 (1994), pp. 126–137.

[32] J. Shi, C. Hu, and C.-W. Shu, *A technique of treating negative weights in WENO schemes*, J. Comput. Phys., 175 (2002), pp. 108–127.

[33] C.-W. Shu, *High-order finite difference and finite volume WENO schemes and discontinuous Galerkin methods for CFD*, Int. J. Comput. Fluid Dyn., 17 (2003), pp. 107–118.

[34] P. K. Sweby, *High resolution schemes using flux limiters for hyperbolic conservation laws*, SIAM J. Numer. Anal., 21 (1984), pp. 995–1011.

[35] B. van Leer, *Towards the ultimate conservative difference scheme*, V. *A second-order sequel to Godunov's method*, J. Comput. Phys., 32 (1979), pp. 101–136.

[36] A. Voss, *Exact Riemann Solution for the Euler Equations with Nonconvex and Nonsmooth Equation of State*, Ph.D. thesis, Technical University of Aachen, Aachen, Germany, 2004.

[37] B. Wang and H. Glaz, *Second Order Godunov-Like Schemes for Gas Dynamics with a Nonconvex Equation of State*, AIAA Report AIAA-99-3256, AIAA, Reston, VA, 1999.

[38] B. Wendroff, *The Riemann problem for materials with nonconvex equations of state.* I. *Isentropic flow*, J. Math. Anal. Appl., 38 (1972), pp. 454–466.

[39] B. Wendroff, *The Riemann problem for materials with nonconvex equations of state.* II. *General flow*, J. Math. Anal. Appl., 38 (1972), pp. 640–658.

[40] A. L. Zachary, A. Malagoli, and P. Colella, *A higher-order Godunov method for multidimensional ideal magnetohydrodynamics*, SIAM J. Sci. Comput., 15 (1994), pp. 263–284.